J. Fluid Mech. (2004), *vol.* 510, *pp.* 219–242.
DOI: 10.1017/S0022112004009486 Printed in the United Kingdom

Flow past a trapezoidal tab

By SUCHUAN DONG† AND HUI MENG‡

Department of Mechanical & Aerospace Engineering, SUNY at Buffalo, Buffalo, NY 14260, USA

(Received 12 July 2002 and in revised form 4 March 2004)

The flow passing over a trapezoidal tab mounted on a flat plate is studied using direct numerical simulation (DNS). Such a tab has been used to generate hairpin-like vortices to enhance cross-stream mixing. We attempt to provide a detailed account of the three-dimensional topology and dynamics of the hairpin vortices in the tab wake. Simulations are conducted for three tab inclination angles at Reynolds number $Re = 600$ based on the free-stream velocity and the tab height. A finite-volume discretization scheme involving 2.6×10^6 control volumes is employed for the simulations and the results are compared with PIV experimental data. Simulations captured all the experimentally observed near-field flow features including a pair of streamwise co-rotating vortices and its transition to hairpin vortices. Simulation results provide new insight into the vortex dynamics in the tab wake. It is shown that the hairpin vortex is capable of lifting up and entraining vorticity from the local boundary layer, thereby increasing its strength to counter the vorticity diffusion. It is also observed that the turbulence production is mostly accomplished by the hairpin heads/arches, while the highest kinetic energy is associated with hairpin vortex legs. The topological characteristics of the structures and the statistical characteristics of the flow are discussed in detail.

1. Introduction

The use of vortex-generating tabs is a common method for mixing enhancement (Reeder & Samimy 1996; Foss & Zaman 1999). The most frequently used tabs are of rectangular and triangular shapes, and have been applied in jets (Bradbury & Khadem 1975; Tanna 1977; Samimy, Zaman & Reeder 1993; Zaman, Reeder & Samimy 1994; Zhang & Schneider 1995; Zaman & Foss 1997) and plane mixing layers (Island, Urban & Mungal 1998; Foss & Zaman 1999). A new class of mixing tabs – the trapezoidal tab – has emerged in recent years. The application of trapezoidal tabs is exemplified by the high-efficiency vortab mixer (Fasano 1991; Etchells, Wadley & Fasano 1999), which consists of an array of such tabs mounted on the inner wall of a pipe or a duct.

Although a trapezoidal tab can be considered as an intermediate geometry between the triangular and the rectangular tab, it bears unique characteristics that facilitate more efficient mixing. In addition to the streamwise vortices found in the wake of a triangular tab (Zaman *et al.* 1994; Reeder & Samimy 1996), the surface-mounted trapezoidal tab also produces a sequence of periodic hairpin-like structures owing to its flat top edge (Gretta & Smith 1993). The hairpin vortices add to the complexity

† Current Address: Division of Applied Mathematics, Brown University, Providence, RI 02912, USA.

‡ Author to whom correspondence should be addressed: huimeng@eng.buffalo.edu.

of the vortex dynamics in the tab wake and offer more efficient mixing mechanisms. Their counter-rotating legs and their arches (or heads) synergistically induce a strong second-quadrant pumping of low-speed fluids from the surface, while their arches also entrain high-speed free-stream fluid into the near-wall region. Once formed, a hairpin vortex moves away from the wall by self-induction (Robinson 1991), making the mixing region grow rapidly. In the presence of nested hairpin vortices, the legs of the preceding hairpin intertwine with the trailing hairpin vortex (Acarlar & Smith 1987*a*). Such interactions cause more energetic mixing in the wake. The pairing and coalescence between hairpin vortices significantly increase the penetration of structures to the outer flow (Gretta & Smith 1993). Furthermore, hairpin structures provide a self-sustaining mechanism by regeneration of secondary hairpin structures through unsteady three-dimensional separation of the surface layer (Smith *et al.* 1991). It is also observed that hairpin structures are long-lived in the tab wake (Yang, Meng & Sheng 2001), persisting until at least 20 tab heights downstream. When the flat top edge of the trapezoidal tab vanishes, the resulting triangular tab produces only a counter-rotating vortex pair and significantly lower cross-stream penetration in a wall-bounded flow (Gretta 1990). Hence, the trapezoidal tab is a more efficient mixing device owing to the unique hairpin vortex dynamics.

The genesis of the surface-mounted trapezoidal tab as a mixing device originated from the study of turbulent boundary layers, wherein hairpin structures and streamwise vortices are believed to perform efficient transport of surface fluid to the outer layer and induce the movement of the outer flow toward the wall (Robinson 1991). Based on observations of both natural turbulent boundary layers and hairpin vortices generated artificially via protrusion or fluid injection on the surface (Acarlar & Smith 1987*a*, *b*; Peridier, Smith & Walker 1991*a*, *b*; Smith *et al.* 1991; Haidari & Smith 1994; Smith & Walker 1995), the trapezoidal tab was devised out of the intent to initiate a turbulent-like flow pattern of hairpin and streamwise vortices at scales in excess of the turbulent boundary layer (Gretta & Smith 1993). The trapezoidal tab is able to create turbulent-like mixing in an otherwise laminar regime and to elevate the turbulence transport levels above those of a natural boundary layer.

Gretta (1990) systematically studied how the geometrical parameters of the trapezoidal tab affect its performance. By using the 'maximum disturbance height', normalized by the tab height, as a measure of the tab mixing efficiency, he observes that increasing the tab length or the overall tab size does not affect the performance significantly, but increasing tab width and decreasing inclination angle results in an increased normalized disturbance height.

Several primary and secondary vortex structures in the wake of the trapezoidal tab were identified in previous experimental work (Gretta & Smith 1993; Elavarasan & Meng 2000; Yang *et al.* 2001). Along with a sequence of hairpin-like structures periodically shed from the tab tip, there is also a pair of counter-rotating streamwise vortices (CVP) in the tab wake. While the conceptual picture of Gretta & Smith (1993) suggests that the two types of vortex coexist in the entire tab wake, Elavarasan & Meng (2000) observed that the CVP and the hairpin vortices dominated different streamwise regions of the wake. The CVP was observed to exist only in the very near tab region. Downstream, it was taken over by hairpin vortices. There was a transitional region in between, where the CVP and the hairpin vortex coexist. Yang *et al.* (2001) reported detailed PIV measurements of the wake of a trapezoidal tab mounted in a turbulent channel. They documented the dynamics of the hairpin vortices observed in two-dimensional slices, several types of hairpin-vortex interactions, the rising of the hairpin heads with downstream distance, the imprints of hairpin vortices on the

mean flow, Reynolds stresses and the turbulence dissipation rate. They observed that hairpin vortices increased strength (circulation) for some distance, and attributed this phenomenon to the pumping of the boundary-layer vorticity by the hairpin vortices. Secondary hairpin vortices were observed in their PIV measurements, along with new kinds of vortices, referred to as reverse vortices, with a sense of rotation opposite to those of the hairpin structures. The secondary hairpin vortices were observed to interact frequently with the primary hairpin vortices (Yang *et al.* 2001). Gretta & Smith (1993) also observed the pairing and coalescence of the primary hairpin vortices and showed that such interactions facilitated the growth of the wake and increased the cross-stream penetration of the structures.

Gretta & Smith (1993), Meng & Yang (1998) and Yang *et al.* (2001) measured the statistics of the trapezoidal tab wake at isolated points or in several discrete planes. It was observed that low mean streamwise velocity and high turbulent intensity coincided with the regions of streamwise vortices. The mean velocity profile exhibited two inflection points, which corresponded to the passage of the hairpin vortex heads and reverse vortices (Yang *et al.* 2001). Because of the technical limitations of the hot-wire anemometry and PIV measurement techniques, the complete turbulence statistics was not given.

The following issues are yet to be addressed pertaining to the dynamics and statistics of the trapezoidal tab wake. How is the counter-rotating vortex pair formed? How are the hairpin vortices generated? How does the CVP transit to the hairpin structures? What is the topological relationship between the two vortex structures in the transitional region? What are the three-dimensional topologies of the hairpin vortices, the secondary hairpin vortices and the reverse vortices observed by Yang *et al.* (2001)? Why are hairpin vortices a long-lived structure in the tab wake despite vorticity diffusion? How is the turbulence production related to the flow dynamics in the wake? Owing to the highly three-dimensional and dynamic nature of the tab flow, these issues were not addressed in previous measurements and visualizations. They subsequently become the motivation of this DNS study.

This work focuses on the near field of the trapezoidal tab wake (within about 5 tab heights). The objectives are to provide a comprehensive physical picture of the trapezoidal tab flow and to elucidate several unresolved questions about the tab wake. Emphasis is placed on the discussion of the vortex dynamics and the statistical characteristics. The understanding gained from this study will be useful for the assessment of the efficiency of the tab mixer and the improvement of its design. Moreover, this work could shed light on the dynamics of the hairpin structures and their roles in turbulent transport in wall-bounded flows.

2. Simulation configuration and methodology

2.1. *Flow configuration*

Figure 1 shows a diagram of the flow. The computational domain has a streamwise length L, a vertical height Q and a spanwise dimension S. All of these parameters are normalized by the tab height h. The trapezoidal tab is mounted on the flat plate with an inclination angle α. The upper edge of the tab is positioned at x_t in the streamwise direction. The geometry parameters of the tab (table 1) including the bottom and top edge widths (a, b), the two tapering angles (β_1, β_2) and the inclination angle are set in accordance with those in PIV experiments (Meng & Yang 1998). We assume that the thickness of the tab is zero throughout the simulations. The direction of the incoming flow is perpendicular to the base of the tab. A structured boundary-fitted grid

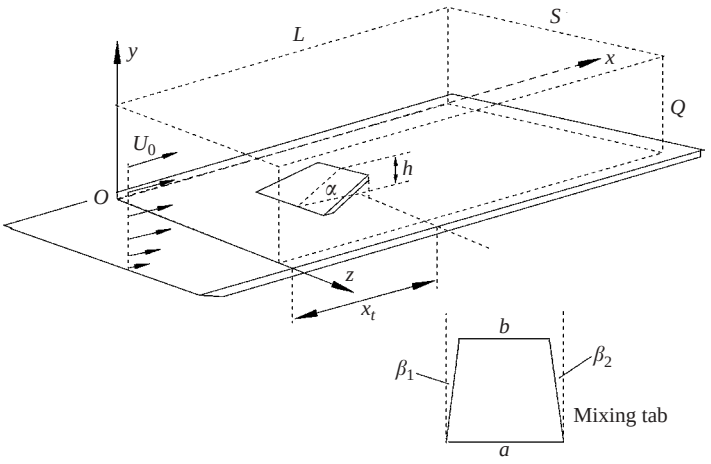

FIGURE 1. Sketch of flow configuration. Dashed box marks the flow domain.

	a (cm)	b (cm)	β_1 (deg.)	β_2 (deg.)	Re	δ/h
PIV/simulation	2.9	2.1	7.6	7.6	600	0.7

TABLE 1. Geometry parameters in both simulation and PIV experiment. See figure 1 for the meanings of symbols.

has been used in current simulations. To resolve the physical characteristics, the grid is clustered around the tab. The flow variables are arranged in a staggered fashion, in which we define the velocities on cell surfaces and the pressure at the cell centre.

2.2. *Computational methodology*

We consider the incompressible Navier–Stokes equations along with the continuity equation:

$$\frac{\partial u_i}{\partial t} + \frac{\partial}{\partial x_j} u_i u_j = -\frac{\partial p}{\partial x_i} + \frac{1}{Re}\frac{\partial}{\partial x_j}\frac{\partial}{\partial x_j} u_i, \tag{1}$$

$$\frac{\partial u_i}{\partial x_i} = 0, \tag{2}$$

where u_i are the velocity components normalized by the free streamwise velocity U_0 and will be used interchangeably with the streamwise, wall-normal and spanwise velocities, (u, v, w); p is the pressure divided by the density and normalized by U_0^2. The spatial coordinates, x_i, have been normalized by the tab height h, and will be used interchangeably with (x, y, z). Thus, the appropriate Reynolds number for this flow is defined as $Re = U_0 h/\nu$, where the kinematic viscosity of the fluid, ν, is assumed to be constant.

The discretization is based on a finite-volume scheme in conjunction with the fractional step temporal differencing of Kim & Moin (1985):

$$\frac{\int \hat{u}_i \,\mathrm{d}v - \int u_i^m \,\mathrm{d}v}{\Delta t} = \tfrac{1}{2}\left(3N_i^m - N_i^{m-1}\right) + \frac{1}{2Re}\left(\oint \boldsymbol{n}\cdot\nabla\hat{u}_i \,\mathrm{d}s + \oint \boldsymbol{n}\cdot\nabla u_i^m \,\mathrm{d}s\right), \tag{3}$$

$$\frac{\int u_i^{m+1}\,\mathrm{d}v - \int \hat{u}_i\,\mathrm{d}v}{\Delta t} = -\oint \phi^{m+1} n_i\,\mathrm{d}s, \tag{4}$$

$$\oint u_i^{m+1} n_i\,\mathrm{d}s = 0, \tag{5}$$

where $\hat{u}_i$ are the intermediate velocity components; u_i^m are the velocity components at time step m. $\boldsymbol{n}$ denotes the outward unit vector of the cell face. The nonlinear term is expressed by $N_i = -\oint u_i \boldsymbol{V}\cdot\boldsymbol{n}\,\mathrm{d}s$, where $\boldsymbol{V}$ is the velocity vector. The pseudo-pressure, ϕ, is related to the pressure p by

$$p = \phi + \frac{\Delta t}{2Re}\nabla^2\phi. \tag{6}$$

The volume and surface integrals in (3) and (4) are evaluated on the grid cell corresponding to u_i, while the surface integral in (5) is evaluated on the grid cell for the pseudo-pressure.

We rearrange the three-dimensional flow variables into vectors. Let U_i and Φ denote the vector forms of the velocities and the pseudo-pressure, respectively. Equations (3)–(5) are then expressed via:

$$A_i \hat{U}_i = R_i \quad (i = 1, 2, 3) \tag{7}$$

$$\left(\sum_{i=1}^{3} D_i C_i^{-1} B_i\right) \Phi^{m+1} = \frac{1}{\Delta t}\sum_{i=1}^{3} D_i \hat{U}_i, \tag{8}$$

$$U_i^{m+1} = \hat{U}_i - \Delta t C_i^{-1} B_i \Phi^{m+1} \quad (i = 1, 2, 3), \tag{9}$$

where A_i are the coefficient matrices for the three velocity components; C_i are diagonal matrices of the cell volumes; B_i are defined by $B_i\Phi = \oint \phi n_i\,\mathrm{d}s$ and D_i are defined by

$$\sum_{i=1}^{3} D_i U_i = \oint \boldsymbol{V}\cdot\boldsymbol{n}\,\mathrm{d}s.$$

The right-hand-side vectors, R_i, are expressed as

$$R_i = \int u_i^m\,\mathrm{d}v + \tfrac{1}{2}\Delta t\left(3N_i^m - N_i^{m-1}\right) + \frac{\Delta t}{2Re}\oint \boldsymbol{n}\cdot\nabla u_i^m. \tag{10}$$

A laminar boundary layer profile with a thickness $\delta = 0.7h$ is prescribed at the inlet. No-slip boundary conditions are imposed on all solid boundaries. A convective boundary condition is applied at the outlet:

$$\frac{\partial u_i}{\partial t} + U_c\frac{\partial u_i}{\partial x} = 0, \tag{11}$$

where U_c is chosen such that the total mass is conserved. Periodic conditions are applied in the spanwise direction. On the upper boundary a no-stress wall condition is used:

$$v = 0, \quad \frac{\partial u}{\partial y} = \frac{\partial w}{\partial y} = 0. \tag{12}$$

2.3. *Parameters*

Three cases are simulated with different inclination angles $\alpha = 12.25°$, $24.5°$ and $49°$, at a fixed Reynolds number $Re = 600$. Table 2 lists the parameters for the three cases.

	α (deg.)	h (cm)	Computational domain
Case A	12.25	0.64	$11.8h \times 3h \times 10.2h$
Case B	24.5	1.24	$10h \times 4h \times 6h$
Case C	49	2.26	$8.7h \times 4h \times 4h$

TABLE 2. Simulated cases.

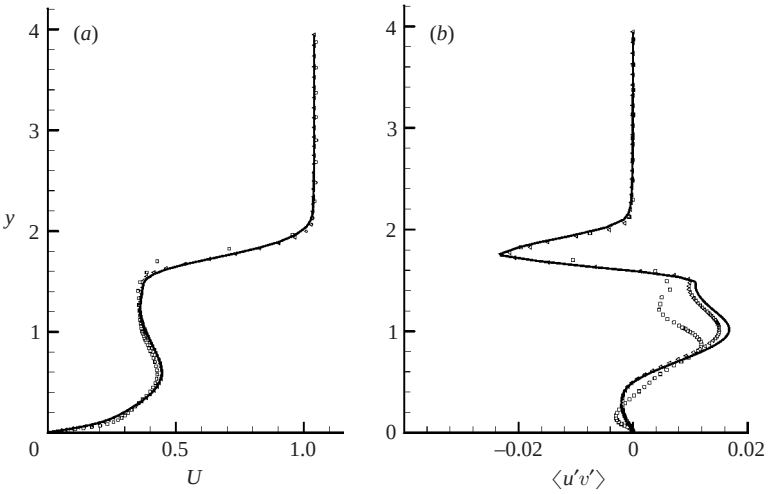

FIGURE 2. (*a*) Mean streamwise velocity U and (*b*) Reynolds stress $\langle u'v' \rangle$ profiles at $x = 8h$ in the centreplane on different grids ($\alpha = 24.5°$). □, $161 \times 65 \times 81$; ◁, $225 \times 97 \times 121$; ——, $225 \times 129 \times 121$.

Based on the inlet friction velocity $u^* = \sqrt{\tau_w/\rho}$ (where τ_w is inlet wall shear stress and ρ is the fluid density) and the viscous length scale $y^* = \nu/u^*$, the first mesh point above the flat plate is approximately at $y^+ = \Delta y_w/y^* \approx 0.23$, and the maximum grid spacing occurs at the upper boundary (free surface) of the domain with $\Delta y^+_{max} = \frac{\Delta y_{max}}{y^*} \approx 4$.

Grid tests were conducted to ensure the sufficiency of the grid resolution. Figure 2 shows the profiles of the mean streamwise velocity U and the Reynolds stress $\langle u'v' \rangle$, where u' and v' are the fluctuating streamwise and wall-normal velocities, in the centreplane obtained on three sets of grids: $161 \times 65 \times 81$, $225 \times 97 \times 121$ and $225 \times 129 \times 121$. With the $225 \times 97 \times 121$ grid, both the mean streamwise velocity and the Reynolds stress are captured correctly with confidence. Therefore, the grid $225 \times 97 \times 121$ is used in all the simulations. The simulation results within the initial 1.5 'flow-through' time ($\approx 1.5L/U_0$, L denoting the length of domain) were discarded to allow for the passage of initial transients. The statistical data set was then accumulated until the flow statistics converged, which amounts to about three 'flow-through' times.

2.4. *Comparison with PIV experiment*

We compare the simulation results with PIV measurements (Meng & Yang 1998) of the tab flow conducted under the same conditions as Case B ($\alpha = 24.5°$). The geometric parameters in the PIV experiments are summarized in table 1.

In figure 3 we plot the mean streamwise velocity $U(y)$ and the Reynolds stress $\langle u'v' \rangle$ profiles at the streamwise location $4.5h$ behind the top edge of the tab in the centreplane. Both simulation and PIV measurement demonstrate a velocity deficit and

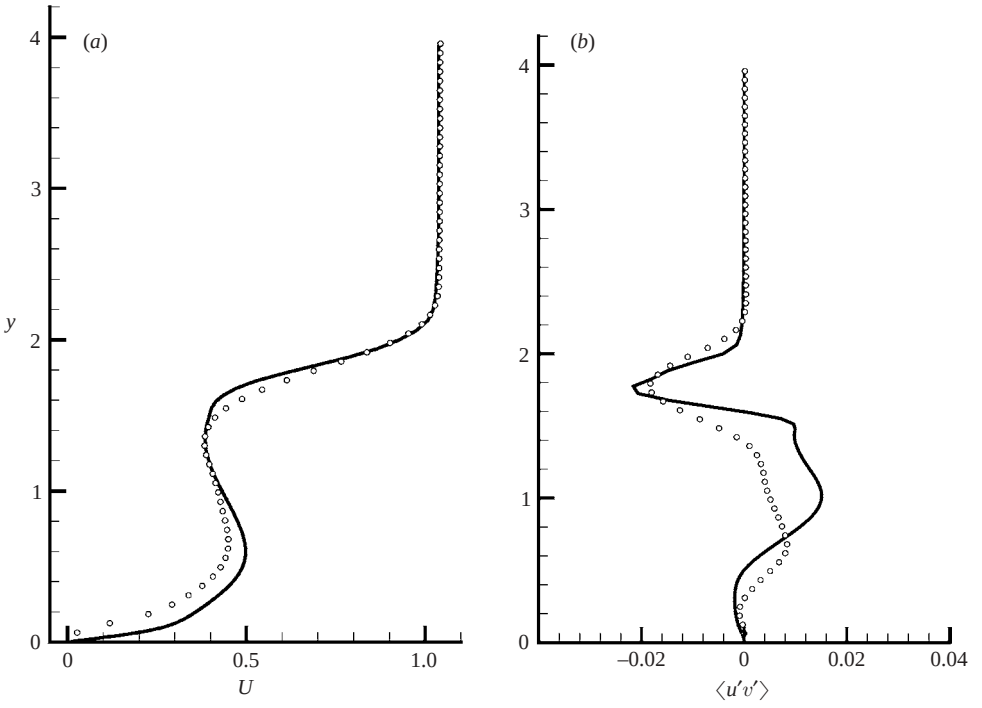

FIGURE 3. Profiles in the centreplane $4.5h$ behind the tab from —, simulation and ○, experiment ($\alpha = 24.5°$): (a) mean streamwise velocity $U(y)$; (b) Reynolds stress $\langle u'v' \rangle$.

two inflection points in the mean velocity profile. Moreover, both simulation and PIV data captured the three distinct layers of Reynolds stress $\langle u'v' \rangle$ with alternating signs along the wall-normal direction. In the middle layer, the simulation over-predicted the Reynolds stress values.

In figure 4, we compare the simulated and measured mean wall-normal velocity V and the Reynolds stress $\langle v'w' \rangle$ profiles. Both the simulation and the experiment produce a zone of positive mean vertical velocity (upward flow) in the middle and zones of negative values (downward flow) on both sides. The upward motion in the middle and the downward motion on the sides are induced by the streamwise rotation of the CVP and hairpin legs. Figure 4(a) further shows a velocity deficit in the profile near the symmetry plane, which is related to the downward induction by the secondary streamwise CVP (see § 3.6). The simulation has captured these characteristics of the mean wall-normal velocity quite well. The profiles of the Reynolds stress $\langle v'w' \rangle$ in figure 4(b) show that the simulation and the PIV measurement have produced the same distributions of the Reynolds stress $\langle v'w' \rangle$. However, on the boundaries of the wake region, the simulation has produced $\langle v'w' \rangle$ values lower than those obtained experimentally, and the width of the wake region (where $\langle v'w' \rangle$ demonstrates significant variations) from the simulation is also smaller than that from the experiment. We believe that these discrepancies came from two sources. First, a zero-thickness tab is assumed in the simulations, while the tab thickness may have a notable influence on the statistics. In the experiment, the finite tab thickness and the sharp corners can induce additional instabilities and fluctuations near the tab edges, which propagate downstream along the boundary of the wake. This will result in larger $\langle v'w' \rangle$ values and a wider wake. Secondly, the fluctuation at the inlet in the experiment may also

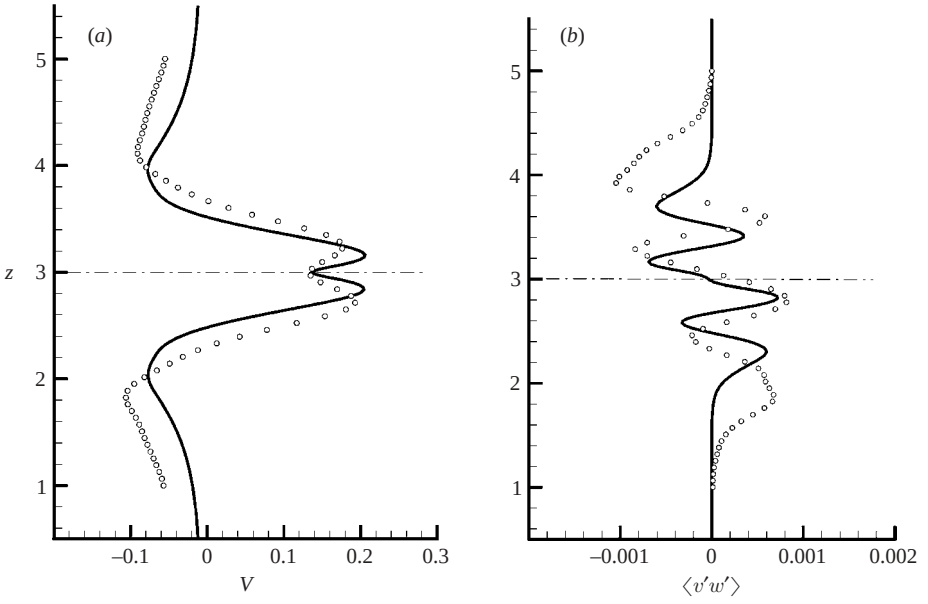

FIGURE 4. Profiles along a horizontal line $4h$ behind the tab and $0.5h$ above the wall from —, simulation and ○, experiment ($\alpha = 24.5°$): (a) mean wall-normal velocity $V(z)$; (b) Reynolds stress $\langle v'w' \rangle$.

have an effect on the obtained statistics of the tab wake. In contrast, no fluctuations are added to the inlet velocity in current simulations. In summary, the overall agreement between the simulation results and the PIV measurements is good.

3. Flow structures

In present simulations, we have confirmed a number of vortex structures and their interaction patterns that were observed in previous experimental studies. In addition, the simulations have revealed several new structures and phenomena in the tab flow such as the upstream necklace vortices, the secondary streamwise counter-rotating vortex pair, and the splitting of the CVP into hairpin vortex legs.

The tab wake comprises a variety of flow structures. In figure 5, we plot the iso-surface of the median eigenvalue, λ_2, of the tensor $\boldsymbol{S}\cdot\boldsymbol{S} + \boldsymbol{\Omega}\cdot\boldsymbol{\Omega}$, where $\boldsymbol{S}$ and $\boldsymbol{\Omega}$ denote the symmetric and the anti-symmetric parts of the velocity gradient tensor, respectively. Jeong & Hussain (1995) define the core of a vortex as a region with two negative eigenvalues, hence requiring $\lambda_2 < 0$. The λ_2 iso-surface seems to have captured overwhelming details, a scenario echoed by Evangelinos & Karniadakis (1999). To illustrate the flow characteristics more clearly, we show the iso-surfaces of the vorticity magnitude $|\boldsymbol{\omega}|$ and the pressure in figures 6(a) and 6(b), respectively. We plot a set of vortex lines together with the vorticity iso-surface. A portion of the hairpin vortex arch is removed to reveal the vortex lines within. Although these distributions are less rigorous than the λ_2 iso-surface as a vortex definition, they provide a simple overview of the main structures in the tab flow.

3.1. *Upstream necklace vortex*

Current simulations reveal the existence of a quasi-stable recirculating necklace vortex (or horseshoe vortex) upstream of the tab, which has not been observed in

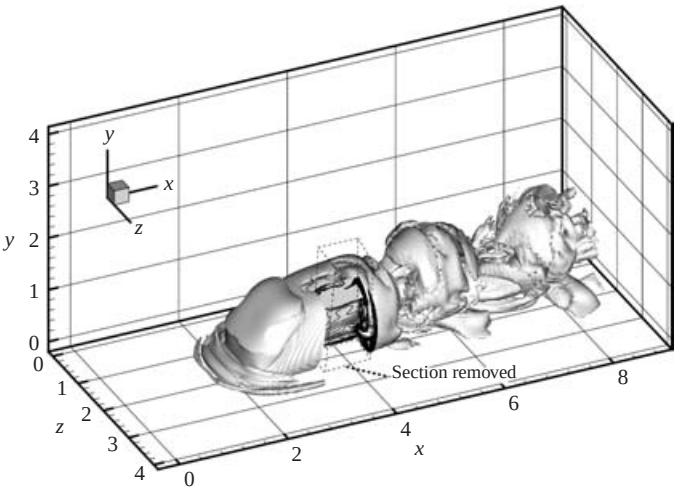

FIGURE 5. Iso-surface $\lambda_2 = -0.1$, where λ_2 denotes the median eigenvalue in Jeong & Hussain (1995). A section behind the tab is removed to show the inner complexities of the structures, with contour lines of λ_2 shown on the cross-sections ($\alpha = 49^\circ$).

previous experiments. Figure 7(*a*) demonstrates this vortex with a set of instantaneous streamlines passing through a horizontal rake at the inlet about $0.3h$ above the flat plate ($\alpha = 49^\circ$). This upstream necklace vortex is also observed for the case $\alpha = 24.5^\circ$, but not for $\alpha = 12.25^\circ$. The dimensions of the necklace vortex are observed to increase as the inclination angle increases. At $\alpha = 49^\circ$ two secondary necklace vortices are observed in front of the original one rotating in contiguous directions (figure 7*b*), similar to those observed in juncture flows (Baker 1979). The necklace vortices encircled the tab. Their legs extend downstream, and gradually lose coherence and disperse into the wake in the far field.

As in many other juncture flows, the necklace vortex forms because the in-coming flow experiences a strong adverse streamwise pressure gradient. This, coupled with the cross-stream pressure gradient generated by the curvature of the flow around the tab, led to a concentration of vorticity (Doligalski, Smith & Walker 1994).

3.2. *Counter-rotating vortex pair*

In the near-tab wake, the flow detours the two side edges and migrates towards the centreplane owing to the pressure difference across the tab. This produces a pair of large streamwise vortices rotating in opposite directions. The contours of the streamwise vorticity ω_x in a cross-stream plane behind the tab (figure 8*a*) clearly show this counter-rotating vortex pair (CVP). The CVP has a dimension comparable to the tab height. The spanwise positions of the vortex cores are approximately at the two side edges of the tab.

The two branches of the CVP originate from the two bottom corners of the tab, with a small lateral dimension initially. By entraining the high-speed fluid into the tab wake, this vortex pair grows rapidly to its full dimension (comparable to h). A projection of the instantaneous traces of the CVP cores onto the (x, y)-plane (figure 8*b*) reveals that the two branches of the CVP almost coincide with each other in height initially, indicating that the CVP is symmetric at the initial stage of development. Above the height $y \approx 0.3h$ (point A in the figure), the two branches begin to rise at different rates until they reach the point (point B in the figure) where

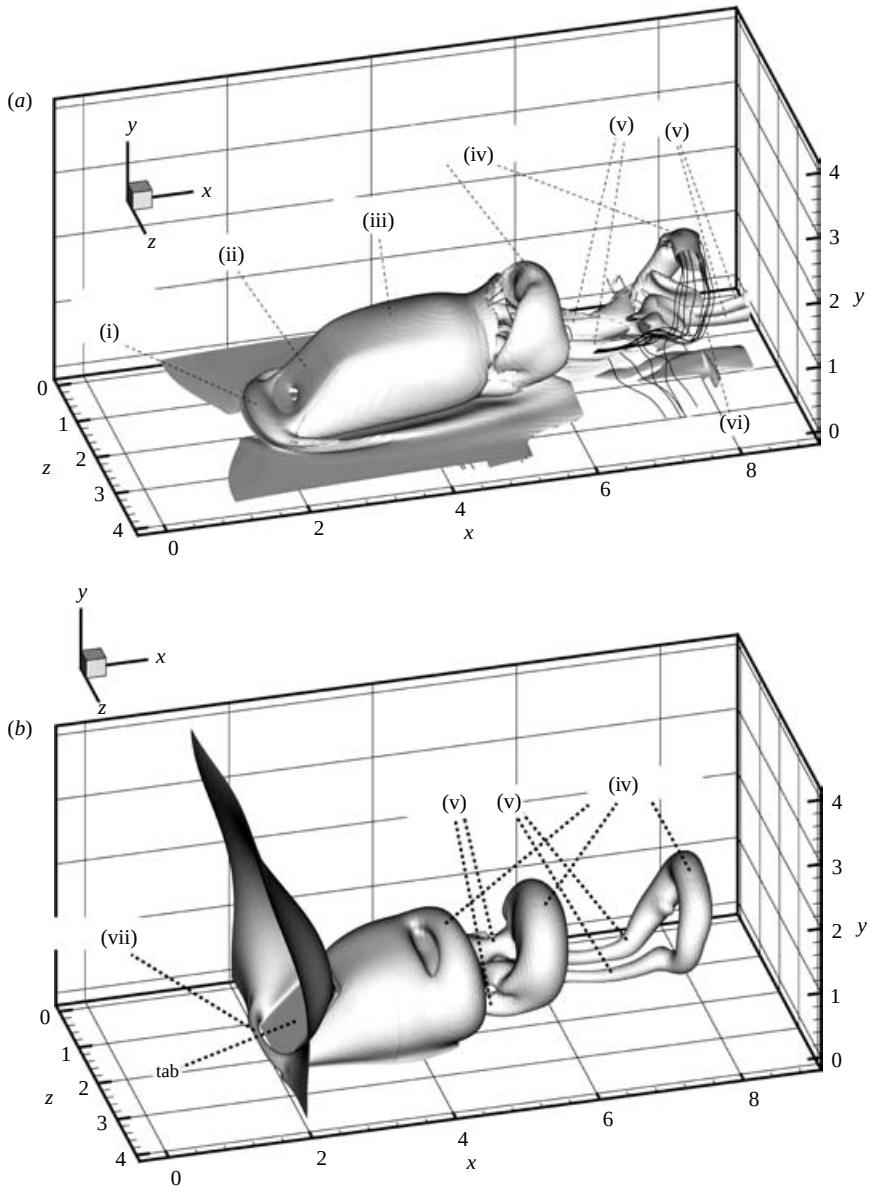

FIGURE 6. Iso-surfaces showing tab wake structures ($\alpha = 49°$). (*a*) Instantaneous vorticity magnitude $|\boldsymbol{\omega}| = 3.5$ and wake vortex lines. A portion of the hairpin vortex arch is removed to reveal the vortex lines within. (*b*) Instantaneous pressure $p = -0.16$. (i) Upstream necklace vortex; (ii) position of tab; (iii) curved shear layer; (iv) hairpin vortex heads; (v) hairpin vortex legs; (vi) vortex lines; (vii) upstream necklace vortex.

the curved shear layer developing from the tab edges becomes unstable and begins to roll up. Beyond that point, the height of the CVP cores decreases and subsequently the CVP evolves into the legs of hairpin vortices.

Consistent with the observations by Elavarasan & Meng (2000), current simulations show that the CVP exists only in the near-tab region; while further downstream the wake is dominated by a series of hairpin vortices. Elavarasan & Meng observe

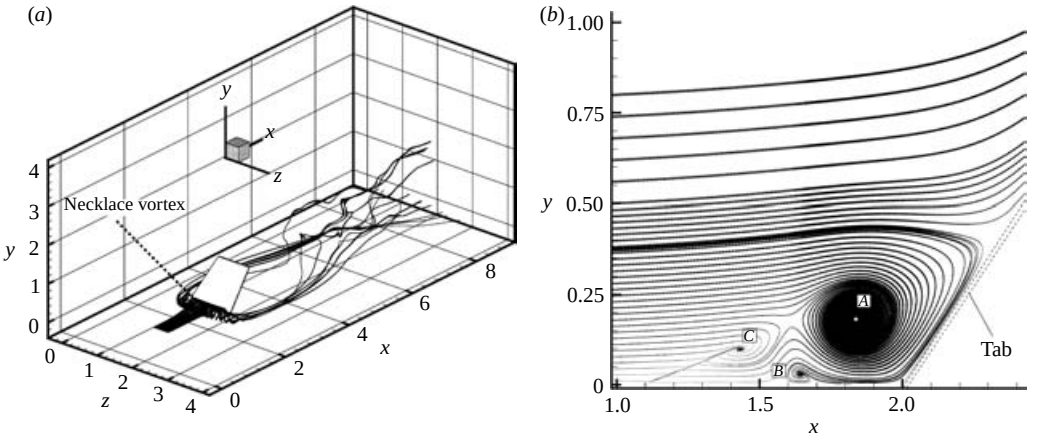

FIGURE 7. Instantaneous streamlines: (*a*) passing through a horizontal rake at the inlet showing upstream necklace vortex (or horseshoe vortex); (*b*) in the centreplane showing primary (*A*) and secondary (*B* and *C*) necklace vortices.

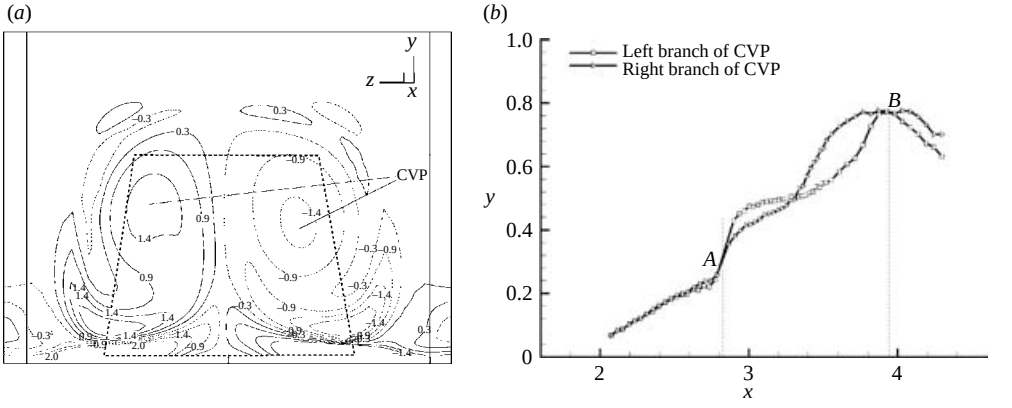

FIGURE 8. Counter-rotating vortex pair (CVP) ($\alpha = 49°$). (*a*) Contours of instantaneous streamwise vorticity ω_x in the cross-stream plane $x = 3.3h$. Heavy dashed line marks the edge of the tab. (*b*) Projection of the instantaneous traces of CVP cores on the (x, y)-plane. □, left-hand, ▷, right hand branches of the CVP. *A*, point where CVP increases dimension rapidly; *B*, point where curved shear layer becomes unstable and begins to roll up.

a transition region in the wake where the CVP and the hairpin vortices co-exist. However, the topological relationship between these two structures was not understood from their experiments. In current simulations, we observe that the CVP evolves into the legs of hairpin vortices through a deformation and splitting process in the transition region. This process is illustrated by the instantaneous two-dimensional streamlines in several cross-stream planes behind the tab (figure 9). Between h and $2h$ behind the tab, the CVP begins to deform and the dimension of the vortex increases. Between $1.5h$ and $2.5h$ behind the tab, the deformation continues and each branch of the CVP splits into two co-rotating vortices. By examining the velocity vector plots and the vorticity iso-contours in various cross-stream planes and various streamwise-wall normal planes, we have determined that the spawned streamwise vortices are topologically the legs of subsequent hairpin vortices. Vortex splitting has

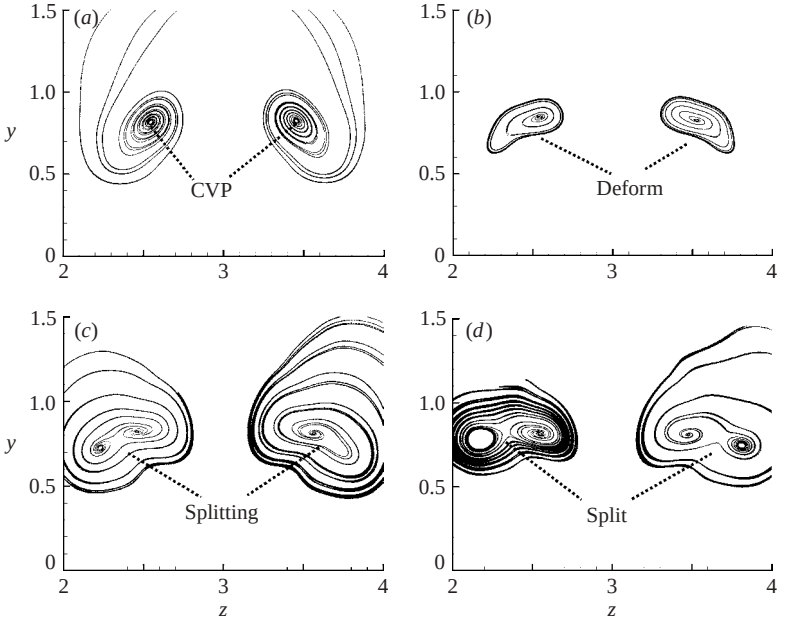

FIGURE 9. Instantaneous two-dimensional streamlines ($\alpha = 24.5°$) in four cross-stream planes with distances behind the tab: (*a*) 1.3*h*, (*b*) 1.6*h*, (*c*) 1.8*h* and (*d*) 1.9*h*, showing the splitting of CVP into hairpin vortex legs.

been observed experimentally in rotating fluids (see Beckers & Heijst 1998), which is due to the growth of the instability on an isolated monopolar vortex. Depending on the disturbances, the monopolar vortex can split into two (dipole splitting) or three vortices (tripolar splitting). The splitting of the counter-rotating vortex pair behind the tab is attributed to the instability associated with the vortex. In the near-tab wake, each branch of the CVP is analogous to a quasi-monopolar vortex. The instability created by the difference of vorticity magnitude in the vortex core and the ambient fluid, together with the disturbances generated by the vortex shedding, causes the splitting of the CVP in the tab wake.

3.3. *Hairpin vortices*

Hairpin vortices, shed into the wake quasi-periodically from the tab, are the dominant structures in the tab wake. They are generated from the three-dimensional curved shear layer wrapping around the tab edges (figure 6*a*). This shear layer is stable within a short distance (1.2*h* for $\alpha = 49°$) behind the tab. Owing to Kelvin–Helmholtz instability, the shear layer rolls up into a series of vortices, each with a 'head' (from the top edge) and two 'legs' (from the two sides). As a shed vortex is convected downstream, its legs are stretched owing to the velocity gradient normal to the flat plate. Eventually, the vortex evolves into a hairpin-like structure. The process of shear roll-up and vortex shedding is evident from figure 10, which shows contours of the instantaneous spanwise vorticity ω_z in the centreplane. The heads of hairpin vortices move farther away from the wall as they travel downstream. In figure 11(*a*) we plot the contours of the instantaneous streamwise vorticity ω_x in the cross-stream plane at $x = 5.3h$. In figure 11(*b*), we plot the streamwise vorticity contours together with the iso-surface of the vorticity magnitude in three-dimensional space. It is evident that these patterns demonstrate the cross-section of the hairpin vortex legs. Similar to the

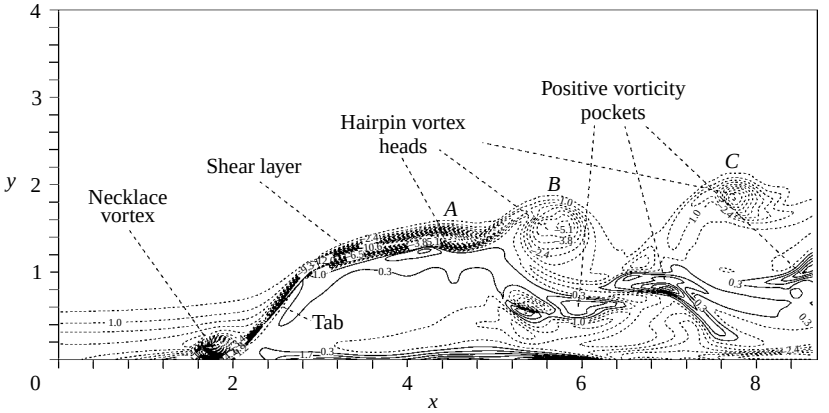

FIGURE 10. Contours of instantaneous spanwise vorticity ω_z in the centreplane ($\alpha = 49°$).

CVP, hairpin vortex legs also entrain ambient high-speed fluid into the wake and generate strong upward pumping between the legs, promoting the cross-stream mixing.

The source of vorticity in hairpin vortices is visualized through the tab-wake vortex lines in figure 12. The portion of the vortex lines outside the wake region resides deep inside the flat-plate boundary layer. These vortex lines form three arched clusters A, B and C, which coincide with hairpin vortices demonstrated by the vorticity iso-surface in figure 6(a). Tracing their origins, we observe that some of the vortex lines in the arches have quasi-streamwise legs, thus taking the hairpin-like shape. These vortex lines may extend all the way to the tab, which indicates that the vorticity was initially lifted from the wall by the tab and were transported downstream. Other vortex lines in the arches are Ω-shaped and extend to the wall at the local streamwise locations, which indicates that the vorticity was lifted up locally from the flat-plate boundary layer.

To explore the relationship between the Ω-shaped vortex and the hairpin vortex, in figure 13 we re-plot the vortex lines passing through hairpin arch C. Figure 13(a) illustrates typical Ω-shaped vortex lines that feature an arch and two inward kinks. In figures 13(b) and 13(c), we plot two horizontal rakes of vortex lines. By rake we refer to a line segment that the vortex lines cross, that is, the vortex lines pass through the points on the rake. The two horizontal rakes are placed in the centreplane (above the centre of the hairpin vortex head C) at $y = 2h$ and $y = 1.92h$, respectively. Since the centre of the hairpin vortex head is at $y = 1.84h$ (as determined from the contours in figure 10), the higher rake (figure 13b) traces the region farther away from the hairpin vortex core, while the lower rake (figure 13c) traces the region closer to the hairpin vortex core. Clearly, the latter case comprises vortex lines with more stretched legs. Our explanation is as follows. As the vorticity is newly lifted up by the hairpin vortex, the vortex line takes the Ω-shape. As the vorticity is transported downstream, the Ω-shaped vortex lines (and kinks) are stretched to join the hairpin vortex legs and the vorticity is entrained into the hairpin vortex. As a result, the 'boundary' region of a hairpin vortex is associated with newly entrained vorticity (corresponding to Ω-shaped vortex lines, see figure 13b), while the central part of a hairpin vortex contains 'older' vorticity entrained upstream (corresponding to vortex lines with more stretched legs, see figure 13c). Figure 13(d) shows the mechanism by which a hairpin vortex pumps, stretches and entrains vorticity from the boundary layer. The arch of the Ω-shaped vortex lines is formed by the Q2 pumping (here Q2 refers to motions

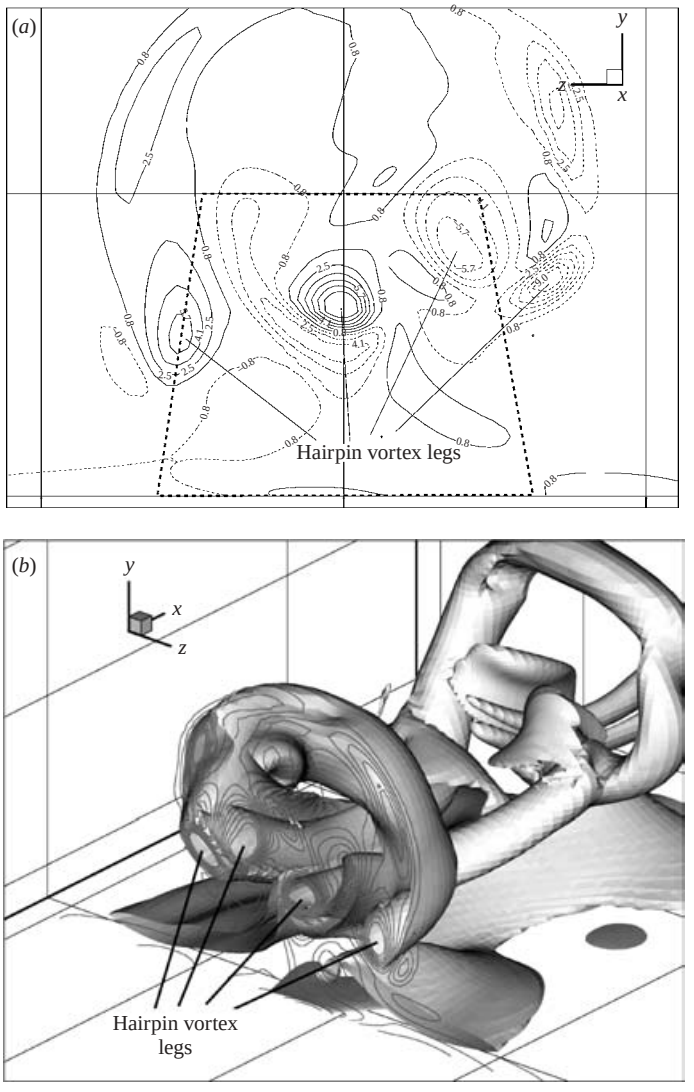

FIGURE 11. Hairpin vortex legs ($\alpha = 49°$). (*a*) Contours of instantaneous streamwise vorticity ω_x in the cross-stream plane at $x = 5.3h$; (*b*) perspective view of spanwise vorticity contours at $x = 5.3h$ together with the iso-surface of vorticity magnitude.

with $u'v'$ in the second quadrant based on the quadrant-splitting scheme introduced by Wallace, Eckelmann & Brodkey 1972; Q1–Q4 events in the following sections refer to motions with $u'v'$ in corresponding quadrants) inside the hairpin vortex, while the inward kinks are generated by induction of the hairpin legs.

Hence, we conclude that the hairpin vortex comprises concentrated vorticity (see the clustered vortex lines) that are pumped up from the wall at various downstream locations along its passage. Correspondingly, the vortex lines are initially Ω-shaped, and are gradually stretched into the hairpin-like shape downstream.

The pumping and entrainment of boundary-layer vorticity by hairpin vortices explain the increase in the vortex strength (circulation) of hairpin heads along the streamwise direction in the tab wake observed by Yang *et al.* (2001). They postulated

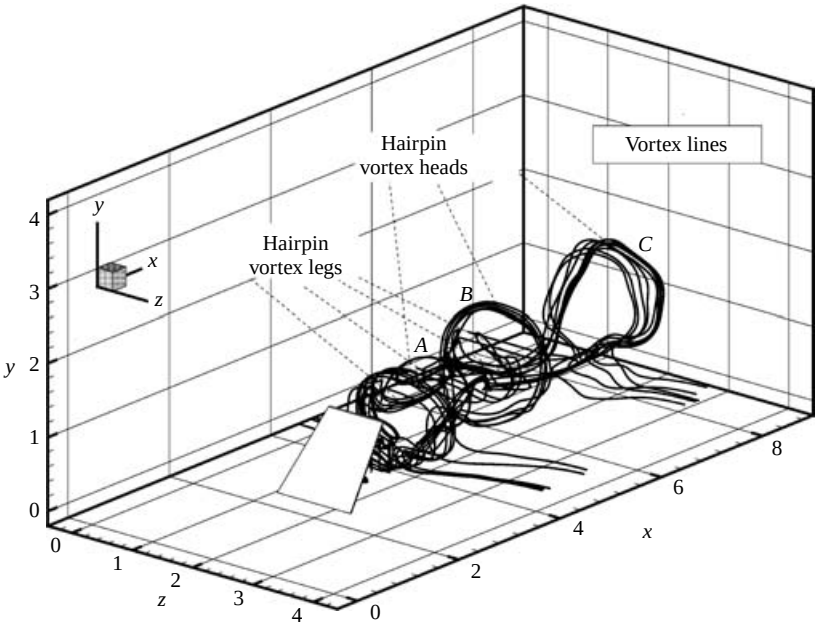

FIGURE 12. Instantaneous vortex lines in tab wake ($\alpha = 49°$).

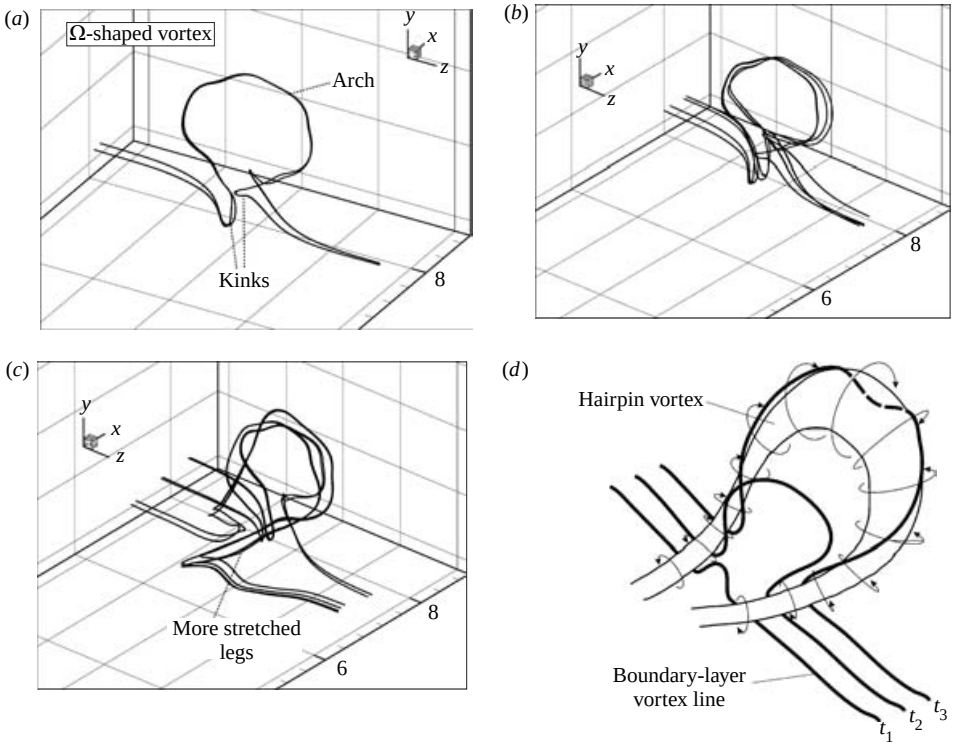

FIGURE 13. Ω-shaped vortex: (*a*) two vortex lines passing through hairpin arch *C* of figure 12 showing features of the Ω-shaped vortex; (*b*) vortex lines passing through a rake placed at $0.16h$ above the centre of hairpin arch *C* of figure 12; (*c*) vortex lines passing through a rake placed at $0.08h$ above the centre of the hairpin arch *C* of figure 12; (*d*) diagram showing the pumping and entrainment of boundary-layer vorticity by a hairpin vortex at successive time instants t_1, t_2 and t_3 ($t_1 < t_2 < t_3$).

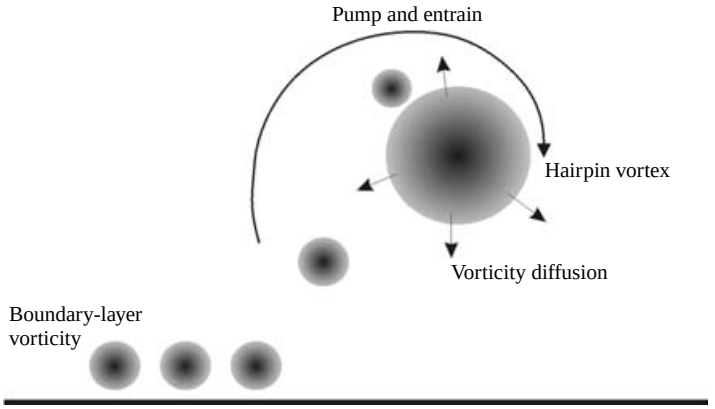

FIGURE 14. Sketch showing the pumping and entrainment of local boundary-layer vorticity by the hairpin vortex. This process increases the hairpin vortex strength and counters the vorticity diffusion.

that the growth of the hairpin strength was due to the pumping of boundary-layer vorticity. The current vortex-line visualization supports this mechanism. Owing to its unique topology, a hairpin vortex near the wall synergistically pumps up (ejects) low-speed fluid from the boundary layer via induction. It is thus able to lift up and entrain new vorticity from the local boundary layer, and increase its strength to counter vorticity diffusion (see the illustration in figure 14). This characteristic could provide a self-sustaining mechanism for the hairpin structure, which explains why hairpin structures are long-lived in the tab wake, persisting until at least 20 tab heights downstream (Yang *et al.* 2001).

The interactions of hairpin vortices are illustrated in figure 15 with a temporal sequence of contours of the instantaneous spanwise vorticity ω_z in the centreplane, where the hairpin heads are marked A, B, C and D. We examine the pairing of two consecutive hairpin vortices marked B and C. Starting from the instant $t = 1.65$ (figure 15*e*), the trailing vortex C travels faster than B. Over the next two instants, vortex C catches up with and rises above B. At $t = 3.63$ (figure 15*h*) these two vortices merge into one denoted by BC. The vertical scale of the wake increases significantly as a result of this pairing process. The pairing of hairpin vortices facilitates both the growth of the wake and the vertical penetration of the structures into the outer flow (Gretta & Smith 1993).

3.4. *Opposite-signed vortex*

Figure 10 also reveals pockets of positive vorticity distributed below the hairpin vortex heads. The portion of figure 10 surrounding the second pocket is enlarged and shown in figure 16(*a*). A vortex with an opposite sense of rotation was identified below and between the two hairpin vortex heads. To make sure that the vorticity characteristics did not arise from inadvertent factors, we slid the viewing plane (streamwise-wall normal plane) along the z-axis and confirmed that this opposite-signed vortex persisted for a significant distance in the spanwise direction.

To trace the opposite-signed vortex in three-dimensional space, we observe that the majority of the vortex lines passing through this vortex core belong to a Ω-shaped bundle associated with a hairpin vortex, as shown in figure 16(*b*). Clearly, the opposite-signed vortex is merely the upper branch of the kink in the Ω-shaped vortex discussed in § 3.3. It results from the vorticity pumping by the hairpin vortex.

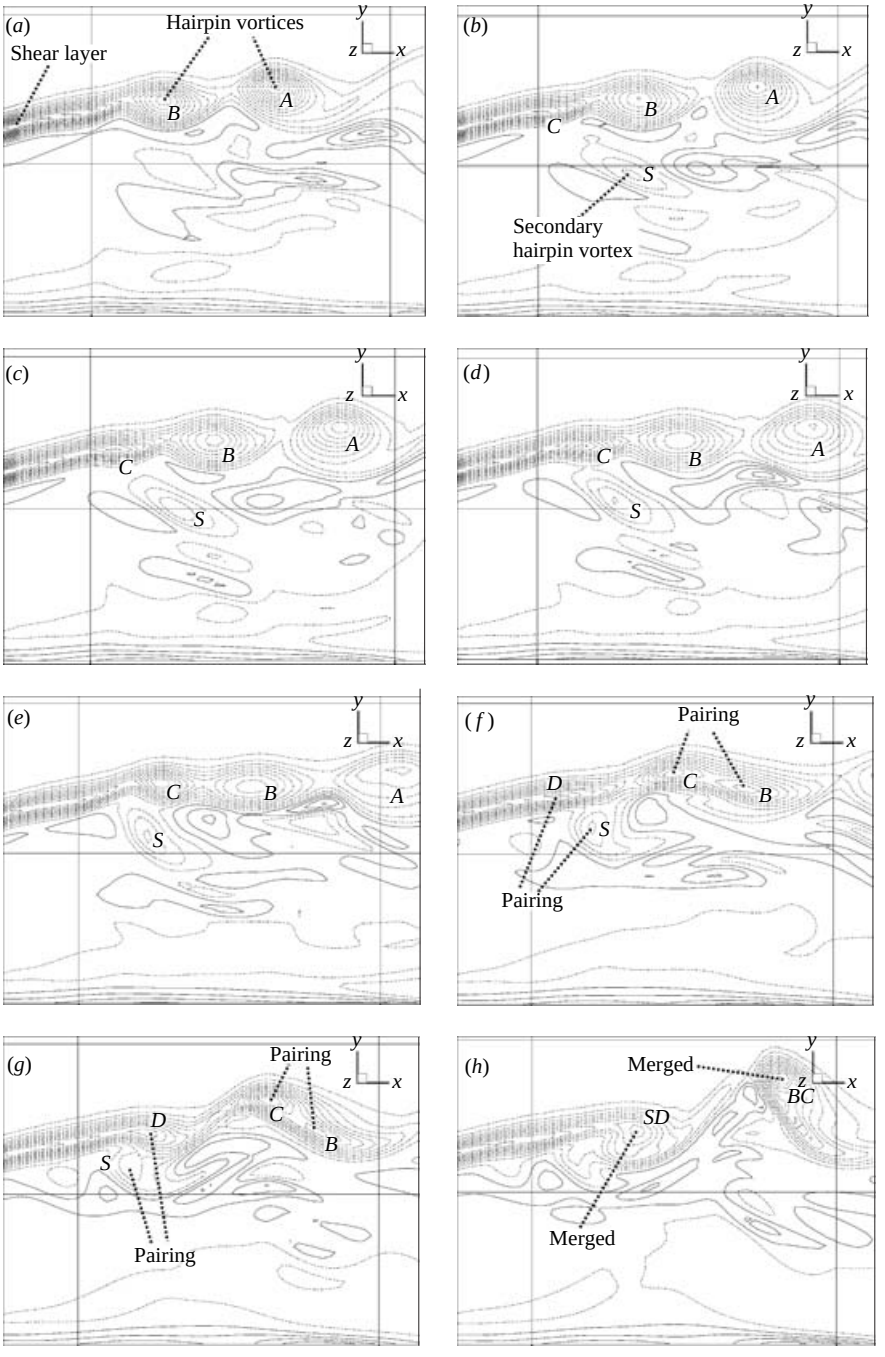

FIGURE 15. A time sequence of contours of instantaneous spanwise vorticity ω_z in the centreplane ($\alpha = 49°$): (*a*) $t = 0$; (*b*) 0.44; (*c*) 0.77; (*d*) 1.1; (*e*) 1.65; (*f*) 2.46; (*g*) 3.03; (*h*) 3.63. The time is in non-dimensional units h/U_0. Dashed lines denote negative values.

In previous PIV measurements (Meng & Yang 1998; Yang *et al.* 2001), a type of vortex called 'reverse vortex' (rotating in a sense opposite to the hairpin heads) was frequently observed below the hairpin heads in the centreplane. In two dimensions,

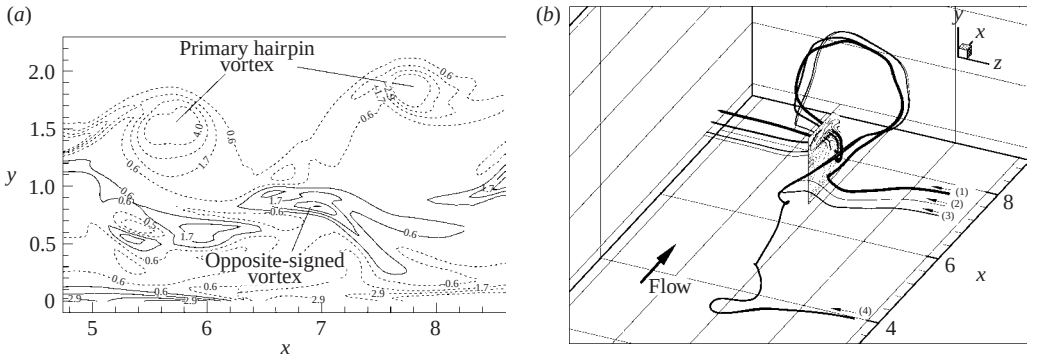

FIGURE 16. Opposite-signed vortex. (*a*) Contours of instantaneous spanwise vorticity ω_z in the centreplane. (*b*) Instantaneous vortex lines passing through the opposite-signed vortex in (*a*). A portion of the spanwise vorticity contours in the centreplane is also shown.

these vortices appear very similar to the opposite-signed vortices seen in current simulations. Yang *et al.* (2001) interpreted the reverse vortex as a secondary structure developed from a reverse shear formed by the interaction of the decelerated fluid below a hairpin head and faster fluid further underneath. This is not inconsistent with the current observation that the opposite-signed vortex is a Ω-shaped vortex pumped and deformed (kinked) by the hairpin. However, it should be pointed out that the experiments covered a much larger streamwise distance of the wake (about $20h$) than current simulations (about $5h$) and that most of the 'reverse vortices' were observed in downstream distances beyond the simulation domain. Yang *et al.* (2001) noticed that for the 'reverse vortices' to be observed, the hairpin heads must be far enough away from the wall.

3.5. *Secondary hairpin vortex*

Those vortex structures formed directly by the tab such as the hairpin vortices and the CVP are referred to as primary vortices, whereas new vortices spawned by the primary vortices are referred to as secondary vortices. In the temporal series shown in figure 15, hairpin vortices A, B, C and D are rolled up from the shear layer formed by the tab edge and hence are primary hairpin vortices, while vortex S is born inside the wake rather than shed from the tab. Hence, vortex S is a secondary structure. According to Yang *et al.* (2001), the unstable shear layer that produces S is generated through the ejection of the preceding hairpin vortex A.

Simulation results demonstrate that the newborn vortex S in figure 15 takes a hairpin-like shape. In figure 17, we plot contours of the spanwise vorticity ω_z in the centreplane including the secondary vortex S (figure 17*a*). We also plot contours of the wall-normal vorticity component ω_y in a horizontal plane at $y = h$ (figure 17*b*). By sliding the vertical viewing plane along the z-axis and the horizontal viewing plane along the y-axis in the simulated data, we confirm that these two sets of contours do denote the same vortices. These vortices are hairpin-shaped. Both views show a series of primary hairpin vortices and the secondary hairpin vortex S inside the primary ones. It is revealed from the three-dimensional flow data that the legs of the secondary hairpin vortex in figure 17(*b*) merge into the legs of the primary hairpin vortices at $y = 0.76h$. The secondary hairpin vortex has the same sense of rotation as the primary ones.

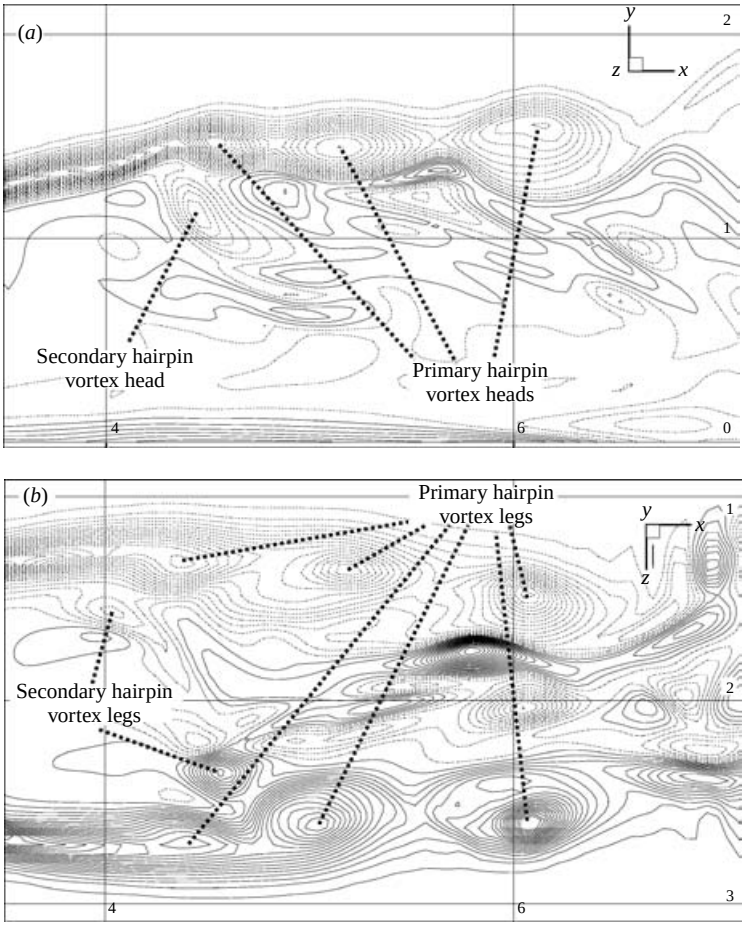

FIGURE 17. Contours of vorticity showing the secondary hairpin vortex: (*a*) spanwise vorticity ω_z in the centreplane; (*b*) wall-normal vorticity ω_y in a horizontal plane at $y = h$. Dashed lines denote negative values.

Using the concept of vorticity pumping discussed in § 3.3, we suggest that the vorticity of the secondary hairpin vortex comes from the flat-plate boundary layer. As the primary hairpin arch is far away enough from the wall, the vorticity of the Ω-shaped vortex lifted up by the hairpin vortex may cluster to form a secondary hairpin vortex due to local instability, instead of being entrained into the primary hairpin vortex. The legs of the secondary hairpin vortex merge into those of the primary hairpins as a result of the stretching of the Ω-shaped vortex downstream. This process is consistent with the vortex-induced boundary-layer breakdown concept proposed by Peridier *et al.* (1991*a*, *b*) and supported by Yang *et al.* (2001).

Current simulation also confirms the observation by Yang *et al.* (2001) that secondary hairpin vortices travel slower than the primary hairpin vortices and merge with the upstream primary hairpin vortices. Since the secondary hairpin *S* is below and inside the primary hairpins, the induced motion by the primary vortices retards the secondary hairpin vortex. This is as shown by the temporal series in figure 15. At $t = 3.03$ (figure 15*g*), *S* starts to pair with the primary hairpin *D*. They merge into a single hairpin vortex marked as *SD* in figure 15(*h*).

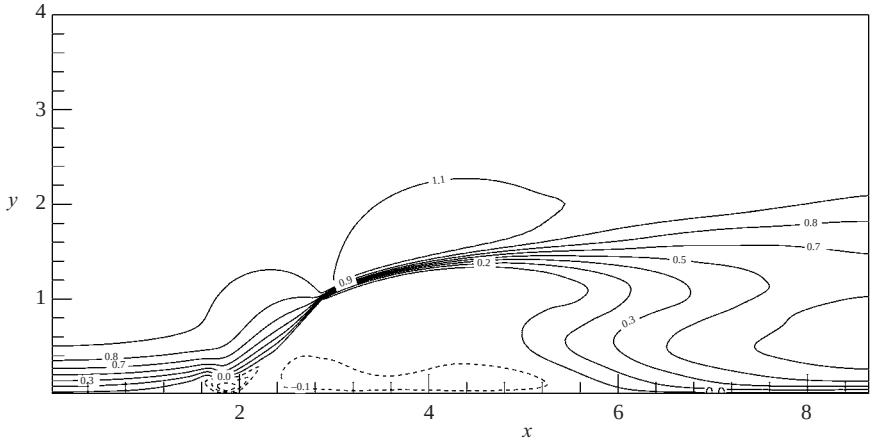

FIGURE 18. Mean streamwise velocity $U(\alpha = 49^\circ)$ contours in the centreplane.

3.6. *Secondary streamwise counter-rotating vortex pair*

Another type of secondary structure, not observed in prior studies, is the secondary streamwise counter-rotating vortex pair. The secondary streamwise CVP is found below the hairpin legs with signs of rotation opposite to those of the primary CVP and the hairpin legs. The secondary streamwise CVP originates near the flat plate in the centreplane at a streamwise location about $2h$ behind the tab top edge. It creates a relatively isolated region of low-momentum fluid near the centreplane in the vicinity of the flat plate. The secondary CVP generates a downward motion near the flat plate, which precludes the low-speed boundary-layer fluid in this region from being transported to the free stream. This interrupts the momentum exchange channel between the boundary layer and the free stream. Therefore, the presence of this secondary streamwise CVP is detrimental to the overall mixing efficiency of the tab mixer.

4. Flow statistics

Statistical analysis of the simulation data is performed to further explore the characteristics of the tab flow. In figure 18, we plot contours of the mean streamwise velocity U in the centreplane. Upstream of the tab, a zone of back flow shows the imprint of the necklace vortices. Higher up, the in-flow deflects over the tab and accelerates along the windward surface, reaching a maximum streamwise velocity about $0.5h$ behind the tab tip. Behind the tab, the flow enters the low-pressure wake, generating a region of recirculating backward flow. This recirculating region becomes more confined to the flat plate with a smaller inclination angle. The notable characteristic of the mean flow is a deficit in the mean streamwise velocity profile. The positive (principal) shear layer above and the negative (reverse) shear layer below the deficit have been demonstrated by Yang *et al.* (2001) to coincide with the passage of the hairpin vortex heads and the opposite-signed vortices, respectively.

The distribution of the Reynolds stress $\langle u'v' \rangle$ in the tab wake (figure 19) shows three distinct layers along the wall-normal direction. The upper layer of negative $\langle u'v' \rangle$ values coincides with the principal mean shear layer ($\partial U/\partial y > 0$) and the passage of hairpin heads in the instantaneous vortex dynamics. The negative $\langle u'v' \rangle$ values indicate that the ejection and sweeping effects (Robinson 1991) induced by hairpin vortex heads are statistically significant. The middle layer of positive $\langle u'v' \rangle$ values

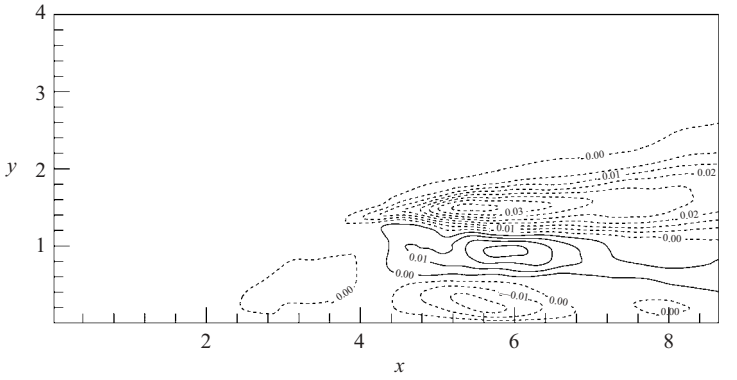

FIGURE 19. Contours of Reynolds stress $\langle u'v' \rangle$ in the centreplane ($\alpha = 49°$).

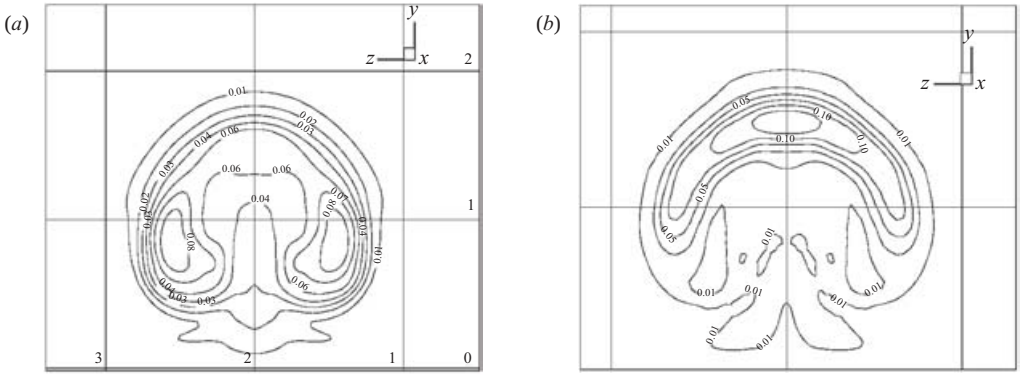

FIGURE 20. Contours of (*a*) kinetic energy and (*b*) production in the cross-stream plane at $x = 5.3h$.

coincides with the reverse shear layer ($\partial U/\partial y < 0$) and the region where the legs of hairpin vortices are active. Also found in this region are opposite-signed vortices. The lowest layer in the Reynolds stress distribution, immediately next to the wall, is of negative $\langle u'v' \rangle$ again, which coincides with the positive shear layer near the wall ($\partial U/\partial y > 0$). The only vortex structure occupying this region is the secondary streamwise CVP. The negative values suggest that the secondary streamwise CVP mostly tilts upward.

The distribution of the kinetic energy, $k = \frac{1}{2}\langle u'^2 + v'^2 + w'^2 \rangle$ (where u', v' and w' denote the streamwise, wall-normal and spanwise fluctuation velocities, respectively), in the centreplane reveals two strips of high fluctuation, each with a local maximum. The upper strip coincides with the principal mean shear and the passage of hairpin vortex heads, while the lower strip coincides with the reverse mean shear. Figure 20(*a*) shows the kinetic energy contours in a cross-stream plane at $x = 5.3h$. Higher kinetic energy is observed in the region occupied by hairpin vortex legs, while in the region of hairpin heads and arches the kinetic energy is relatively low. This observation is consistent with the measured result by Gretta & Smith (1993).

In figure 20(*b*), we plot contours of the turbulence production

$$P_t = -\sum_{i=1}^{3}\sum_{j=1}^{3} \langle u_i' u_j' \rangle \frac{\partial U_i}{\partial x_j}$$

(with U_i denoting mean velocity components) in the cross-stream plane at the same streamwise location. High production is observed in a curved shell region, corresponding to the passage of the hairpin vortex arches in three-dimensional space. This indicates that hairpin vortex arches, as opposed to hairpin vortex legs, provide most of the turbulence production.

5. Mixing

The role of various vortices in the fluid mixing process in the tab wake is considered from two aspects: (i) mixing between the wake and the ambient fluid, and (ii) mixing inside the wake. The wake here is roughly defined as the three-dimensional shell spanned by the hairpin vortices and the CVP. The mixing between the wake and the ambient fluid is attributed to the hairpin vortices and, in the near-wake, the CVP. High-speed fluid from outside is entrained into the wake, while near-wall low-speed fluid inside the wake is pumped up into the outer flow. Such pumping action is accomplished by both the strong Q2 ejection of hairpin vortex heads and the common-up pumping of the CVP and the hairpin legs. The pairing and coalescence of hairpin vortices further enhances the mixing between the wake and the ambient fluid by dramatically increasing the wake growth.

The hairpin vortices and the CVP are also responsible for the mixing inside the wake, which is further enhanced by the secondary hairpin vortices. The secondary streamwise CVP, however, hampers the overall mixing by interrupting the momentum exchange between the near-wall region and the free-stream flow with its common down motion, which is opposite to the motion caused by the primary CVP and the hairpin vortices. Finally, the upstream necklace vortices do not apparently participate in the mixing process in the wake.

The tab inclination angle has a notable effect on the mixing. In the three cases simulated, the largest inclination angle produces the highest level of fluctuation. The pressure drop across the tab also increases as the inclination angle increases. The simulation suggests that a larger tab inclination angle produces a better mixing, but at the expense of a larger pressure drop across the tab, hence requiring more power to drive the flow. Gretta (1990) employed the normalized disturbance height, which was defined as the maximum height at which the disturbance to the hydrogen bubble sheet in the experiment by the flow structures could still be felt, as a measure of mixing efficiency. He observed that in the far field, larger normalized disturbance heights were associated with smaller tab inclination angles, while in the near field (in the range covered by current simulations) no significant differences were observed in the normalized disturbance height for various angles. In present simulations, if we define a disturbance height as the location with a mean streamwise velocity of 99% of the free-stream velocity, our results also show similar disturbance heights for the three angles.

6. Concluding remarks

This is the first DNS study of the flow past a trapezoidal tab, which has both fundamental and technological relevance. Although the current study is concentrated on the near-tab wake, all flow structures in the wake are initiated in this region. The interactions and evolution of these structures not only exhibit tremendous complexity, but also play a crucial role in the physics of mixing and far-wake behaviour. The direct numerical simulations have clarified a number of previous

experimental observations, revealed new topological and dynamical details of vortex structures, and addressed some open questions regarding the mechanisms and dynamic processes of the structures. We summarize the important points from this study below:

(i) Two basic structures in the wake, namely the counter-rotating vortex pair and the hairpin vortices, are topologically related. It is known that hairpin arches are initiated from the unstable shear layer formed on the edges of the tab. Our study further reveals that the CVP, originating from the bottom corners of the tab, evolves into the hairpin vortex legs through a deformation and splitting process.

(ii) The hairpin vortex comprises concentrated vorticity that is lifted up from the wall region at various streamwise locations. Pumped up by an existing hairpin vortex, the newly elevated wall vorticity forms an Ω-shaped vortex. The Ω-shaped vortex is subsequently entrained into the hairpin vortex and stretched into the hairpin-like shape as it is advected downstream.

(iii) Since hairpin vortex pumps up and entrains new vorticity from the local boundary layer, it is able to increase its strength to counter vorticity diffusion. This explains the longevity of hairpin vortex structures observed in previous experiments (Yang *et al.* 2001).

(iv) 'Reverse vortex' (rotating in a sense opposite to the hairpin heads) found in previous experiments (Yang *et al.* 2001) as a separate structure in the far wake region is not observed in current simulations. However, in the near field of the tab wake, an opposite-signed vortex is found and identified as a part of the Ω-shaped vortex, pumped and kinked by the hairpin.

(v) There is a strong correlation between the dynamics of the vortical structures and the statistical characteristics of the tab wake. Turbulence production is mostly accomplished by the hairpin vortex arches, while the highest turbulent kinetic energy is associated with the hairpin vortex legs.

The authors are indebted to Professor Peyman Givi for numerous invaluable discussions, and to Professor Rodney O. Fox for helpful discussions during the early stage of the project. This work was supported by the National Science Foundation under Grant CTS-9625307. Computer time was provided by the National Center for Supercomputing Applications (NCSA) at the University of Illinois at Urbana Champaign and the Center for Computational Research (CCR) at the State University of New York at Buffalo.

REFERENCES

Acarlar, M. S. & Smith, C. R. 1987*a* A study of hairpin vortices in a laminar boundary layer. Part 1. Hairpin vortices generated by a hemisphere protuberance. *J. Fluid Mech.* **175**, 1–41.

Acarlar, M. S. & Smith, C. R. 1987*b* A study of hairpin vortices in a laminar boundary layer. Part 2. Hairpin vortices generated by fluid injection. *J. Fluid Mech.* **175**, 43–83.

Baker, C. J. 1979 The laminar horseshoe vortex. *J. Fluid Mech.* **95**, 347–367.

Beckers, M. & Heijst, G. J. F. 1998 The observation of a triangular vortex in a rotating fluid. *Fluid Dyn. Res.* **22**, 265–279.

Bradbury, L. J. S. & Khadem, A. H. 1975 The distortion of a jet by tabs. *J. Fluid Mech.* **70**, 801–813.

Doligalski, T. L., Smith, C. R. & Walker, J. D. A. 1994 Vortex interactions with walls. *Annu. Rev. Fluid Mech.* **26**, 573–616.

Elavarasan, R. & Meng, H. 2000 Flow visualization study of role of coherent structures in a tab wake. *Fluid Dyn. Res.* **27**, 183–197.

Etchells, A. W., Wadley, R. & Fasano, J. B. 1999 Gas-gas mixing with Kenics HEV mixer: inlet and outlet effects. *North American Mixing Forum, Mixing Conference XVII, Alberta, Canada.*

Evangelinos, C. & Karniadakis, G. 1999 Dynamics and flow structures in the turbulent wake of rigid and flexible cylinders subject to vortex-induced vibrations. *J. Fluid Mech.* **400**, 91–124.

Fasano, J. B. 1991 Kenics HEV mixer sets a new standard for turbulent mixing efficiency. *North American Mixing Forum, Mixing Conference XIII, Alberta, Canada.*

Foss, J. K. & Zaman, K. B. M. Q. 1999 Large- and small-scale vortical motions in a shear layer perturbed by tabs. *J. Fluid. Mech.* **382**, 307–329.

Gretta, W. J. 1990 An experimental study of the fluid mixing effects and flow structure due to a surface mounted passive vortex generating device. MS thesis, Department of Mechanical Engineering, Lehigh University, Bethlehem, PA.

Gretta, W. J. & Smith, C. R. 1993 The flow structure and statistics of a passive mixing tab. *J. Fluid Engng* **115**, 255–263.

Haidari, A. H. & Smith, C. R. 1994 The generation and regeneration of single hairpin vortices. *J. Fluid Mech.* **277**, 135–161.

Island, T. C., Urban, W. D. & Mungal, M. G. 1998 Mixing enhancement in compressible shear layers via sub-boundary layer disturbances. *Phys. Fluids* **10**, 1008–1020.

Jeong, J. & Hussain, F. 1995 On the identification of a vortex. *J. Fluid Mech.* **285**, 69–94.

Kim, J. & Moin, P. 1985 Application of a fractional-step method to incompressible Navier–Stokes equations. *J. Comput. Phys.* **59**, 308.

Meng, H. & Yang, W. 1998 Dynamics of hairpin vortices in the wake of a surface mounted mixing tab. *13th US Congress of Appl. Mech. Gainesville, FL, 21–26 June.*

Peridier, V. J., Smith, F. T. & Walker, J. D. A. 1991*a* Vortex-induced boundary-layer separation. Part 1. The unsteady limit problem $Re \rightarrow \infty$. *J. Fluid Mech.* **232**, 99–131.

Peridier, V. J., Smith, F. T. & Walker, J. D. A. 1991*b* Vortex-induced boundary-layer separation. Part 2. Unsteady interacting boundary-layer theory. *J. Fluid Mech.* **232**, 133–165.

Reeder, M. & Samimy, M. 1996 The evolution of a jet with vortex-generating tabs: real-time visualization and quantitative measurements. *J. Fluid Mech.* **311**, 73–118.

Robinson, S. K. 1991 Coherent motions in the turbulent boundary layer. *Annu. Rev. Fluid Mech.* **23**, 601–639.

Samimy, M., Zaman, K. B. M. Q. & Reeder, M. F. 1993 Effect of tabs on the flow and noise field of an axisymmetric jet. *AIAA J.* **4**, 1251–1258.

Smith, C. R. & Walker, J. D. A. 1995 Turbulent wall-layer vortices. In *Fluid Vortices* (ed. S. Green), chap. 6, pp. 235–290. Kluwer.

Smith, C. R., Walker, J. D. A., Haidari, A. H. & Sobrun, U. 1991 On the dynamics of near-wall turbulence. *Phil. Trans. R. Soc. Lond.* A **336**, 131–175.

Tanna, H. K. 1977 An experimental study of jet noise, Part II: shock associated noise. *J. Sound Vib.* **50**, 429–444.

Wallace, J. M., Eckelmann, H. & Brodkey, R. S. 1972 The wall region in turbulent shear flow. *J. Fluid Mech.* **54**, 39–48.

Yang, W., Meng, H. & Sheng, J. 2001 Dynamics of hairpin vortices generated by a mixing tab in a channel flow. *Exps. Fluids* **30**, 705–722.

Zaman, K. B. M. Q. & Foss, J. K. 1997 The effect of vortex generators on a jet in a cross flow. *Phys. Fluids* **9**, 106–114.

Zaman, K. B. M. Q., Reeder, M. F. & Samimy, M. 1994 Control of an axisymmetric using vortex generators. *Phys. Fluids* **6**, 778–793.

Zhang, S. & Schneider, S. P. 1995 Quantitative molecular-mixing measurements in a round jet with tabs. *Phys. Fluids* **7**, 1063–1070.